Atmos. Chem. Phys., 24, 5585–5602, 2024
https://doi.org/10.5194/acp-24-5585-2024

Atmospheric Chemistry and Physics
Open Access
EGU

Research article

Modeling the influence of carbon branching structure on secondary organic aerosol formation via multiphase reactions of alkanes

Azad Madhu, Myoseon Jang, and Yujin Jo

Engineering School of Sustainable Infrastructure and Environment,
University of Florida, Gainesville, FL 32608, USA

Correspondence: Myoseon Jang (mjang@ufl.edu)

Received: 18 April 2023 – Discussion started: 23 June 2023
Revised: 16 February 2024 – Accepted: 6 March 2024 – Published: 15 May 2024

Abstract. Branched alkanes represent a significant proportion of hydrocarbons emitted in urban environments. To accurately predict the secondary organic aerosol (SOA) budgets in urban environments, these branched alkanes should be considered as SOA precursors. However, the potential to form SOA from diverse branched alkanes under varying environmental conditions is currently not well understood. In this study, the Unified Partitioning Aerosol Phase Reaction (UNIPAR) model is extended to predict SOA formation via the multiphase reactions of various branched alkanes. Simulations with the UNIPAR model, which processes multiphase partitioning and aerosol-phase reactions to form SOA, require a product distribution predicted from an explicit gas kinetic mechanism, whose oxygenated products are applied to create a volatility- and reactivity-based α_i species array. Due to a lack of practically applicable explicit gas mechanisms, the prediction of the product distributions of various branched alkanes was approached with an innovative method that considers carbon lengths and branching structures. The α_i array of each branched alkane was primarily constructed using an existing α_i array of the linear alkane with the nearest vapor pressure. Generally, the vapor pressures of branched alkanes and their oxidation products are lower than those of linear alkanes with the same carbon number. In addition, increasing the number of alkyl branches can also decrease the ability of alkanes to undergo autoxidation reactions that tend to form low-volatility products and significantly contribute to alkane SOA formation. To account for this, an autoxidation reduction factor, as a function of the degree and position of branching, was applied to the lumped groups that contain autoxidation products. The resulting product distributions were then applied to the UNIPAR model for predicting branched-alkane SOA formation. The simulated SOA mass was compared to SOA data generated under varying experimental conditions (i.e., NO_x levels, seed conditions, and humidity) in an outdoor photochemical smog chamber. Branched-alkane SOA yields were significantly impacted by NO_x levels but insignificantly impacted by seed conditions or humidity. The SOA formation from branched and linear alkanes in diesel fuel was simulated to understand the relative importance of branched and linear alkanes with a wide range of carbon numbers. Overall, branched alkanes accounted for a higher proportion of SOA mass than linear alkanes due to their higher contribution to diesel fuel.

Published by Copernicus Publications on behalf of the European Geosciences Union.

1 Introduction

Secondary organic aerosol (SOA) in the atmosphere, formed via the atmospheric oxidation of various precursor hydrocarbons (HCs), serves a considerable role in climate, cloud formation, and human health (Nel, 2005; Shrivastava et al., 2017; World Health Organization, 2016; U.S. EPA, 2019). Precursor HCs found in ambient air are emitted through a variety of both anthropogenic and biogenic sources. Alkanes are one of the major classes of precursor HCs typically found in urban environments, emitted from anthropogenic sources such fossil fuels, personal care products, paints, and pesticides (Li et al., 2022; Wu et al., 2019). In addition to anthropogenic sources, plant wax has also been identified to be a significant source of alkanes present in SOA (Alves et al., 2012). Alkanes do not represent a large proportion of biogenic emissions relative to other biogenic volatile organic compounds (VOCs), but they tend to be large, low-volatility compounds which can still significantly contribute to SOA (Männistö et al., 2023; Lyu et al., 2017). Several recent gas sampling studies have identified alkanes, alongside aromatics, as one of the two dominant sets of HCs measured in urban environments (Massolo et al., 2010; Song et al., 2019; Xuan et al., 2021; Zhao et al., 2020). For example, from their review of various VOC sampling studies, Song et al. (2019) reports that alkanes represent between 40.3 % and 74.4 % of VOCs in a set collected from Houston, Mexico, and various urban cities in China. Within the set of alkanes in their study, Song et al. (2019) found that branched alkanes represented 33 % of alkanes sampled in Langfang, China. This is consistent with the work of Caplain et al. (2006), who reported that linear and substituted alkanes represent significant proportions of both gasoline and diesel fuel exhaust at 6 %–18 % and 18 %–31 %, respectively. Additionally, recent regional modeling studies have shown that alkanes are also one of the dominant sources of SOA formation in urban environments (Li et al., 2022; Jo et al., 2024; Yang et al., 2019). Within the set of alkanes, branched alkanes represent larger proportions of both gasoline and diesel fuels compared with linear alkanes (Gentner et al., 2012). Furthermore, intermediate-volatility organic compounds (IVOCs) in the atmosphere are largely composed of an unresolved complex mixture, which is likely to consist of a variety of branched-alkane isomers (Tkacik et al., 2012).

Currently available mechanisms of branched alkanes are either overly simplistic, with a limited set of oxidation products (Lim and Ziemann, 2009), or overly complex, with too many products to be incorporated into an SOA model (i.e., GECKO-A). Some studies have managed to model the SOA formation of various branched alkanes using the GECKO-A model (Aumont et al., 2013; La et al., 2016). However, because the number of oxidation products in the GECKO-A model increases exponentially as the number of carbons of the HC precursor increases, these studies had significant limitations as they tried to reduce the number of products to a manageable value. For example, La et al. (2016) reduced the number of products considered in the model by limiting the experimental time to a maximum of 1 h. Aumont et al. (2013) reduced the number of precursors considered by only considering the high-NO_x condition, a limitation which they acknowledge is a "severe simplification". For application to a regional model, parameters generated from chamber models must be applicable to a variety of NO_x conditions for the whole range of oxidation products generated throughout a long oxidation time.

In a recent chamber study by Madhu et al. (2023), the SOA formation of a series of linear alkanes was simulated for a wide range of carbon numbers using the Unified Partitioning Aerosol Reaction (UNIPAR) model, which simulates SOA mass via multiphase reactions of HCs. The UNIPAR model utilizes an α_i array generated from explicitly predicted gas oxidation products. The volatility- and reactivity-based lumped species in the array are applied to multiphase partitioning and aerosol-phase reactions to form SOA mass (Choi and Jang, 2022; Han and Jang, 2022; Im et al., 2014; Yu et al., 2021b; Zhou et al., 2019). In order to predict SOA mass originating from linear alkanes at different carbon lengths, an incremental volatility coefficient (IVC) was used to predict the α_i arrays of larger linear alkanes without explicit mechanisms (Madhu et al., 2023). In their model simulation, the importance of low-volatility autoxidation products in linear-alkane SOA formation was demonstrated.

The molecular structure of an alkane serves an important role in its capability to form SOA mass. Linear and branched alkanes tend to have similar oxidation products, with the distinction that branched-alkane products tend to be more volatile at the same precursor carbon number (Lim and Ziemann, 2009). Additionally, the presence of some alkyl branches can decrease the ability of alkanes to participate in autoxidation reactions and increase the decomposition of intermediate products, which further reduces SOA yields by decreasing the amount of low-volatility oxidation products formed. As NO_x decreases in polluted urban areas, the contribution of low-volatility autoxidation products becomes relatively more important in SOA formation (Pye Havala et al., 2019; Praske et al., 2018). In this study, the UNIPAR model is used to simulate the SOA formation from the multiphase reactions of branched alkanes. Due to a lack of practically applicable explicit gas mechanisms, the product distributions of branched alkanes were constructed primarily using the product distributions of linear alkanes with the nearest vapor pressure. To account for the reduction in the probability for autoxidation reactions, an autoxidation reduction factor, which is a function of the degree of branching and position, was applied to the construction of lumped groups that include autoxidation products. Predicted α_i arrays for various branched alkanes (isododecane; 2,6,10-trimethyldodecane; 2,2,4,4,6,8,8-heptamethylnonane; and 2,4,6,10-tetramethylpentadecane) were used to simulate SOA formation, which was compared to chamber-generated

SOA data. The sensitivity of branched-alkane SOA yields to humidity, NO_x conditions, seed conditions, and branching structure under given simulation conditions was projected. Additionally, a simulation of SOA formation from branched and linear alkanes found in diesel was used to determine their relative significance as SOA precursors.

2 Experimental section

Alkane SOA was produced from photooxidation of a set of branched alkanes – isododecane (80 %; Sigma-Aldrich), trimethyldodecane (99 %; Sigma-Aldrich), heptamethylnonane (98 %; Sigma-Aldrich), and tetramethylpentadecane (95 %; Fisher Scientific) – using the Atmospheric PHotochemical Outdoor Reactor (UF-APHOR) dual chamber (52 m^3 each) located at the University of Florida. A detailed description of the operation of the large outdoor smog chamber can be found in a previous study (Im et al., 2014). Table 1 summarizes the experimental conditions of outdoor chamber experiments. Precursor alkane HCs were injected into the chamber through evaporation via heating. CCl_4 ($\geq$ 99.5 %; Sigma-Aldrich) was introduced into the chamber as a nonreactive gas that is used to measure chamber dilution. HONO was used as a source of hydroxyl radicals in the chamber. HCs, HONO, and NO (2 % in N_2; Airgas Inc., USA) and inorganic seed were introduced into the smog chamber before sunrise. Experiments were performed under two different NO_x levels (high NO_x: HC / NO_x < 5 ppbC ppb^{-1}; low NO_x: HC / NO_x > 10 ppbC ppb^{-1}) and three different seed conditions (without seed, sulfuric acid, and ammonium sulfate). Concentrations of gas-phase HCs and CCl_4 were measured using a gas chromatography flame ionization detector (GC-FID, 7820A; Agilent Technologies, Inc., USA). Concentrations of ozone and NO_x within the chamber were measured using a photometric ozone analyzer (400E; Teledyne Technologies, Inc., USA) and a chemiluminescence NO / NO_x analyzer (T201; Teledyne Technologies, Inc., USA), respectively. Experiments using inorganic seed employed a particle-into-liquid sampler (ADISO 2081; Applikon Inc., USA) integrated with ion chromatography (Compact IC 761; Metrohm Inc., Switzerland) (PILS-IC) to measure inorganic ion concentrations within the chamber. The size distribution of particles within the chamber was measured using a scanning mobility particle sizer (SMPS 3080; TSI Inc., USA).

Previous studies that have measured the density of alkane SOA have found a range from 1 to 1.4 g cm^{-3} (Li et al., 2020; Li et al., 2022; Lim and Ziemann, 2009; Loza et al., 2014). Aerosols from each alkane experiment in this study were assumed to have a density of 1.2 g cm^{-3}. A hygrometer (CR1000 measurement and control system; Campbell Scientific Inc., USA) was used to measure meteorological factors (temperature; relative humidity, RH) and an ultraviolet radiometer (TUVR; Eppley Laboratory Inc., USA) was used to measure sunlight intensity. An organic carbon / elemental carbon analyzer (OC / EC model 4; Sunset Laboratory Inc., USA) was used to measure the concentration of organic carbon in aerosol every 50 min. The OC / EC used a nondispersive infrared detector (NDIR) that measured OC using thermal–optical transmittance. The concentration of organic matter (OM, μg m^{-3}) in aerosol was then calculated based on the OC concentration predicted by the UNIPAR model and an OM-to-OC ratio. The OM-to-OC ratio of SOA from alkane species decreased as the chain length increased. The concentrations of OM measured from the chamber were corrected for chamber dilution using a dilution factor and for particle wall loss to the chamber wall using a particle loss factor. An aerosol chemical speciation monitor (ACSM; Aerodyne Research Inc., USA) was used to measure the aerosol composition (sulfate, nitrate, ammonium, and OM). The compositions obtained from the ACSM were compared with measurements from the OC / EC and the PILS-IC. SOA yields (Y) were then calculated as the final measured concentration of OM divided by the total consumption of HC precursors. In order to characterize the chemical functional distribution of SOA, chamber-generated SOA was collected on a silicon disk (13 × 2 mm; Sigma-Aldrich, USA) using a home-built impactor and analyzed using a Fourier-transform infrared (FTIR) spectrometer (Nicolet iS50; Thermo Fisher Inc., USA) in transmission mode. The FTIR disk was weighed using an analytical balance before and after particle impaction to measure particle mass collected.

3 Model description

The efficacy of the UNIPAR model has been demonstrated with respect to simulating SOA formation in photochemical chamber experiments from a variety of HC classes, including aromatic HCs (Im et al., 2014; Zhou et al., 2019; Han and Jang, 2022), monoterpenes (Yu et al., 2021b), and isoprene (Beardsley and Jang, 2016). Furthermore, UNIPAR has been recently integrated into the CAMx regional-scale model and used to demonstrate SOA formation from various HCs including isoprene, terpenes, aromatics, and linear alkanes (Jo et al., 2024; Yu et al., 2022). In this study, UNIPAR model parameters were developed for the simulation of SOA formation from branched alkanes. The UNIPAR model simulates SOA mass formation via the multiphase reactions of HC precursors including gas (g), organic (org) and inorganic (inorg) phases. Typically, the UNIPAR model employs a near-explicit gas oxidation mechanism which is used to create a product distribution for each HC precursor by lumping products into an α_i array consisting of 48 groups according to their volatility and reactivity. An approach using product-structure-based α_i array renders the ability to simulate SOA formation via multiphase partitioning and in-particle chemistry that forms oligomeric products. In addi-

tion to SOA mass, SOA's chemical and physical characteristics, such as the oxygen-to-carbon ratio (O / C) and aerosol viscosity were simulated in the model. Detailed descriptions of lumping criteria and the mass-based stoichiometric coefficient (α_i) of lumped group i as a function of NO_x levels and the degree of aging can be found in previous studies (Madhu et al., 2023; Han and Jang, 2022; Choi and Jang, 2022; Yu et al., 2021b; Zhou et al., 2019). Because of a lack of practically applicable gas oxidation mechanisms for the variety of branched alkanes found in the atmosphere, a novel method was used to create α_i arrays for each branched alkane. Individual branched-alkane α_i arrays were constructed primarily using existing α_i arrays, developed by Madhu et al. (2023), of the linear alkanes with the nearest vapor pressures. To account for the reduction in the autoxidation products created by branched alkanes, an autoxidation reduction factor, which is a function of the degree and position of branching, was applied to lumped groups that contain autoxidation products. Figure 1 shows the UNIPAR model framework. In the presence of inorganic seed, the SOA mass is simulated via three paths: OM produced via multiphase partitioning of organic products (OM_P), aerosol-phase reactions of organic species to form OM_{AR} via oligomerization in the org phase, and reactions in the wet inorg phase which also form OM_{AR} (acid-catalyzed oligomerization and organosulfate, OS, formation).

3.1 UNIPAR model inputs

The parameter inputs to the UNIPAR model for each precursor HC include the equations for α_i and lumped species' physicochemical parameters, such as molecular weight (MW), O / C ratios, and hydrogen bonding (HB). The model inputs associated with each individual experiment include the consumption of HC (ΔHC), the concentrations of alkyl peroxide radical (RO_2) and hydroperoxyl radical (HO_2), concentrations of ionic species (sulfate and ammonium ions), temperature, and humidity. The measured sunlight profile for each experiment is linked to the gas oxidation of each HC yielding ΔHC, [RO_2], and [HO_2]. Gas simulation was performed in the box model platform of Dynamically Simple Model of Atmospheric Chemical Complexity (DSMACC; Emmerson and Evans, 2009) interfaced with the kinetic preprocessor (KPP). The predetermined mathematical equations for stoichiometric coefficients were constructed for linear alkanes using an explicit gas mechanism, as described in the following (Sect. 3.2). For the simulation of SOA mass, HC consumption of branched alkanes was simulated with the Carbon Bond 6 mechanism (CB6r3; Emery et al., 2015). Further details about the CB6 mechanism used in this study can be found in the Supplement (Sect. S1).

Table 1. Summary of experimental conditions and observed data for experiments performed in the UF-APHOR outdoor chamber.

Label	Date (mm/dd/yy)	HC name	Initial NO_x (ppb)	Initial HONO (ppb)	HC initial[a] (ppb)	Seed[b]	HC consumed[c] (ppb)	Final OC ($\mu g\,m^{-3}$)	SOA yield[d]	Comments
C12A	07/08/22	Isododecane	911	100	220	None	76.5	0.7	0.001	Fig. 2
C12B	06/07/22	*n*-Dodecane	829	97	159	None	173.4	19.0	0.024	Madhu et al. (2023); Fig. 3
C12C	06/07/22	*n*-Dodecane	331	200	135	None	131.3	123.2	0.206	Madhu et al. (2023); FTIR, Fig. 4
C15A	07/18/22	Trimethyldodecane	936	140	220	None	162.0	103.8	0.110	Fig. 2
C15B	08/04/22	Trimethyldodecane	607	107	262	SA	161.6	141.2	0.150	Fig. 2
C15C	02/17/22	*n*-Pentadecane	665	117	202	None	125.3	117	0.285	Madhu et al. (2023); Fig. 3
C16A	09/02/22	Heptamethylnonane	433	80	170	None	60.0	3.5	0.006	Fig. 2
C16B	09/02/22	Heptamethylnonane	205	60	165	None	63.0	1.7	0.003	Fig. 2
C16C	04/14/23	Heptamethylnonane	120	90	100	AS	55.3	26.1	0.051	Fig. 2
C16D	04/14/23	Heptamethylnonane	120	90	100	SA	60.6	25.7	0.046	Fig. 2
C19A	07/29/22	Tetramethylpentadecane	260	110	195	None	147.7	447.5	0.276	Fig. 2; FTIR, Fig. 4
C19B	08/09/22	Tetramethylpentadecane	251	100	163	SA	141.4	267.5	0.172	Fig. 2; FTIR, Fig. 4
C19C	08/09/22	Tetramethylpentadecane	232	100	163	NS	140.1	389.7	0.253	Fig. 2
C19D	03/30/23	Tetramethylpentadecane	229	39	39	NS	30.1	79.0	0.239	Fig. 2
C19E	03/30/23	Tetramethylpentadecane	143	73	39	NS	36.1	149.6	0.377	Fig. 2

[a] Initial concentrations of tetramethylpentadecane were calculated using a 95 % injection efficiency, as this compound is too low volatility to be measured by the GC-FID. [b] Experiments were performed with no seed (None) and sulfuric acid seed (SA). [c] Values for the amount of tetramethylpentadecane consumed in each experiment are reported based on model simulations (seen in Fig. S3), as this compound is too low volatility to be measured by the GC-FID. [d] Yield was calculated as the ratio between the concentration of the final measured SOA mass ($\mu g\,m^{-3}$) and the concentration of precursor alkane consumed ($\mu g\,m^{-3}$).

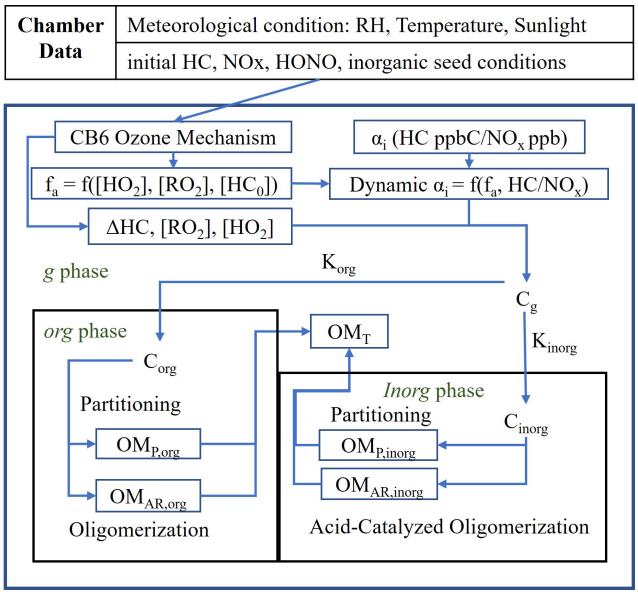

Figure 1. A simplified scheme of the UNIPAR model used in this study. $[HC]_0$ represents the initial hydrocarbon (HC) concentration. Chamber-generated data are used to set initial conditions and the meteorological condition for the gas simulation. The CB6 ozone mechanism is used to simulate the consumption of HC (ΔHC) and the concentrations of hydroperoxide radical ($[HO_2]$) and organic peroxyl radical ($[RO_2]$). The dynamic mass-based stoichiometric coefficients (dynamic α_i) of lumped species i are calculated as a function of HC / NO_x and the aging factor (f_a). f_a is represented as a function of $[HO_2]$, $[RO_2]$, and $[HC]_0$ (Zhou et al., 2019). The gas, organic, and inorganic phases are represented by the subscripts g, org, and inorg, respectively. K_{org} and K_{inorg} represent the partitioning coefficients of lumped species to the org phase and inorg phase, respectively. C_{org} and C_{inorg} represent the concentrations of lumped species in the org and inorg phases, respectively. $OM_{P,org}$ and $OM_{P,inorg}$ represent the mass of organic matter (OM) present in the org and inorg phases, respectively, due to partitioning. $OM_{Ar,org}$ and $OM_{AR,inorg}$ represent the OM formed in the org phase due to in-particle chemistry, such as oligomerization, and in the inorg phase due to acid-catalyzed oligomerization and organosulfate formation (Beardsley and Jang, 2016; Im et al., 2014; Zhou et al., 2019). OM_T represents the total SOA mass formed.

3.2 Gas mechanisms

The atmospheric oxidation of alkanes begins with the reaction with an OH radical, followed by the addition of O_2 to form peroxyl radicals. In the presence of NO_x, these peroxyl radicals can form alkoxy radicals or organonitrate (Finlayson-Pitts and Pitts, 2000). In addition, peroxyl radicals can create hydroperoxides via the reaction with HO_2 radicals. In the previous literature (Crounse et al., 2013; Bianchi et al., 2019; Roldin et al., 2019), terpene peroxyl radicals are capable of undergoing autoxidation reactions to form low-volatility products. These reactions have been previously modeled (Pye Havala et al., 2019; Xavier et al., 2019). In a recent modeling study, Madhu et al. (2023) applied autoxidation mechanisms to improve the prediction of a series of linear-alkane SOA. In their study, the product distribution of linear alkanes with relatively small carbon numbers (C9–C12) were predicted using explicit gas mechanisms which consisted of their respective Master Chemical Mechanism (MCM) and newly added autoxidation mechanisms. The product distributions, associated with stoichiometric coefficients, of the α_i array were extrapolated to larger linear alkanes that do not currently have MCM mechanisms using an incremental volatility coefficient (IVC). The feasibility of the α_i arrays generated with the IVC approach was demonstrated to predict chamber-generated SOA data. For branched alkanes, explicit gas mechanisms are not currently available for the practical application to the UNIPAR SOA model, as described in Sect. 1. In this study, to produce product distributions for the variety of branched alkanes, the preexisting linear-alkane α_i arrays are extrapolated to branched alkanes, as seen in Sect. 3.4 below.

3.3 Lumping structure of the UNIPAR model

As discussed in Sect. 3.2, the α_i array of branched alkanes in the UNIPAR model is inherited from linear alkanes.

The lumping structure of the UNIPAR model, along with a dynamic α_i array that considers aging, has been developed in previous studies (Zhou et al., 2019; Han and Jang, 2020; Yu et al., 2021b). The α_i array is constructed based on products' volatility–reactivity characteristics. The α_i array consists of six different reactivity levels (very fast, VF; fast, F; medium, M; slow, S; partitioning only, P; and multi-alcohol, MA) and eight different volatility levels (1×10^{-8}, 1×10^{-6}, 1×10^{-5}, 1×10^{-4}, 1×10^{-3}, 1×10^{-2}, 1×10^{-1}, and 1.0 mm Hg) based on vapor pressure that represent 48 species. The eight volatility levels have enthalpy of vaporization values of 140×10^3, 106×10^3, 96×10^3, 89×10^3, 82×10^3, 58×10^3, 58×10^3, and 58×10^3 J mol^{-1}, respectively. Further description regarding the basis for the enthalpy of vaporization values can be found in Sect. S2. During the process, each non-radical gas oxidation product of a specific precursor is lumped into 1 of the 48 species. During SOA simulations, all oxidation products within a specific lumped group undergo partitioning, or particle-phase reactions, as single species. For example, consider the compound 3-dodecanol, a product of n-dodecane photooxidation. This compound (3-dodecanol) has a calculated vapor pressure of 5.1×10^{-3} mm Hg (Myrdal and Yalkowsky, 1997; Zhao et al., 1999; Stein and Brown, 1994). Because the vapor pressure is smaller than that of group 7 (1×10^{-2} mm Hg) and larger than that of group 6 (1×10^{-3} mm Hg), 3-dodecanol is lumped into volatility group 6. Due to a lack of functional groups that promote particle-phase reactions (i.e., ketone and aldehyde), 3-dodecanol is lumped into reactivity group P and will only participate in partitioning. This process is performed to lump each non-radical gas oxidation product, with a sufficiently

low vapor pressure, into 1 of the 48 lumped groups. If group 6P contains only 3-dodecanol, then the α value of that group represents the units (i.e., $\mu g\,m^{-3}$) of 3-dodecanol produced per unit of precursor HC consumed. If group 6P has multiple compounds, then the α value of that group represents the sum of the units produced of all products classified under 6P per unit of precursor consumed. After the initial lumping process, the amount of each gas oxidation species produced per unit of HC consumed is extracted via a standardized gas simulation. This gas simulation predicts gas oxidation product concentrations for a given initial precursor concentration at various NO_x levels under a sunlight file near the middle of summer (6 June 2018). These simulation results produce lumped arrays for four different conditions: high NO_x, fresh; high NO_x, aged; low NO_x, fresh; and high NO_x, aged. The α value of each group is represented as a polynomial equation that is a function of the HC ppbC / NO_x ppb level (Table S3 in the Supplement). After α values are calculated for a specific HC ppbC / NO_x ppb level, they can be scaled between fresh and aged compositions, as described below. By doing so, the UNIPAR model is able to leverage the complexity of a relatively large semi-explicit gas oxidation mechanism (generally between 200 and 500 non-radical species per precursor from MCM) while limiting the computational load. In the model, autoxidation products are typically allocated to low-volatility and low-reactivity groups (volatility group 1 in reactivity groups P and S).

Atmospheric aging can augment the product distribution, forming more reactive and less volatile products via oxidation or forming photolysis products that are more volatile but may be more reactive. The stoichiometric coefficients of the α_i array are dynamically predicted as a function of NO_x and aging, as described in previous literature (Zhou et al., 2019; Han and Jang, 2020; Yu et al., 2021b). A weighted aging factor is used to dynamically change α_i values based on fresh and highly oxidized compositions. The aging factor (f_a) at a time t, as detailed in Zhou et al. (2019), is defined as follows:

$$f_a(t) = \log\frac{[HO_2] + [RO_2]}{[HC]_0}, \quad (1)$$

where $[HO_2]$, $[RO_2]$, and $[HC]_0$ are the concentrations of hydroperoxide radical, organic peroxyl radical, and initial HC, respectively. Generally, the amount of oxidation within a given system is correlated with the concentrations of radicals within the system, with higher concentrations of radicals in more aged systems. Thus, concentrations of major radicals, normalized by initial hydrocarbon concentration, are used to represent the amount of aging. Both fresh and highly oxidized α_i arrays are constructed for each NO_x level as well as the respective aging factors. $f_a(t)$ is also used to generate an aging scale that ranges from zero (fresh composition) to one (highly oxidized composition) as follows (Zhou et al., 2019):

$$f'_a(t) = \frac{f_a(\text{highly oxidized}) - f_a(t)}{f_a(\text{highly oxidized}) - f_a(\text{fresh})}. \quad (2)$$

$f'_a(t)$ is calculated for a given NO_x level and used to dynamically calculate the α_i values for that same NO_x level as follows (Zhou et al., 2019):

$$\alpha_i = \left(1 - f'_a(t)\right)(\text{fresh}\alpha_i) + \left(f'_a(t)\right)(\text{highly oxidized }\alpha_i). \quad (3)$$

Essentially, $[HO_2]$ and $[RO_2]$ are used to scale the oxidation product distribution of a given HC precursor (i.e., α_i array) between a fresh and aged composition. Physicochemical parameters of lumping species include MW, the O / C ratio, and HB and are used to calculate multiphase partitioning and in-particle chemistry in the UNIPAR model. Further details about lumping criteria and physicochemical parameters can be found in the study by Zhou et al. (2019).

3.4 Construction of branched-alkane lumping arrays

In the current UNIPAR model, the lumping arrays of a variety of linear alkanes can be predicted using the IVC approach (Madhu et al., 2023). To extend the lumping array of linear alkanes to branched alkanes, the volatility drop caused by branched-alkyl groups was considered by matching each branched alkane to the linear alkane with the nearest vapor pressure. In addition, the lumping array in the model simulates the impact of the degree and position of branched-alkyl groups on reducing the ability of branched alkanes to undergo autoxidation reactions. Supplement Fig. S2 illustrates the ability of branched-alkyl groups to reduce the ability of branched alkanes to undergo autoxidation reactions. For example, *n*-heptadecane has 14 secondary carbons that can undergo autoxidation mechanism, as seen in Fig. S2 (left panel), whereas 2,2,4,4,6,8,8-heptamethylnonane has only 1 secondary carbon that can process autoxidation due to the 7 methyl branches which reduce the number of hydrogens available for abstraction. To account for this, an autoxidation reduction factor (ARF) is applied to the lumping array of branched alkane and calculated as follows:

$$\text{ARF} = \frac{\text{AP of branched alkane}}{\text{AP of linear alkane with nearest vapor pressure}}. \quad (4)$$

Here, the autoxidation potential (AP) can be calculated as follows:

a. Terminal, primary carbons are not included for AP.

b. Carbons that are in the α or β position relative to terminal carbons on the alkane backbone are assigned an AP value of 1, and this carbon can only undergo autoxidation reactions in one direction. For example, this would apply to carbons 2, 3, 14, and 15 in Fig. S2a.

c. Other carbons on the main alkane backbone are assigned an AP value of 2 due to the potential for autoxidation occurring in two directions. For example, this would apply to carbons 4 to 13 in Fig. S2a.

d. If one alkyl branch is present on a carbon, then the AP value is multiplied by 0.5.

e. If geminal alkyl branches are present on a carbon, then the AP value is multiplied by 0.

f. The AP value of each alkane is the sum of all AP values for each carbon.

Further information on the basis for the calculation of the ARF can be found in Sect. S3. ARF in Table S1 summarizes the physical properties and ARF values for branched alkanes used in the chamber experiments of this study. Physicochemical parameters and α values of lumping arrays of compounds used for chamber experiments can be found in Sects. S5 and S6. Ultimately, this approach allows for the reduction of SOA formation found in branched alkanes compared with that in linear alkanes with same carbon numbers.

3.5 SOA formation by multiphase partitioning

The partitioning process of lumping species is fundamental to form SOA and process in-particle chemistry. Partitioning coefficients for each lumping species, i, between g and the org phase ($K_{\mathrm{org},i}$) or between g and the wet inorg phase ($K_{\mathrm{inorg},i}$) are calculated using the typical gas–particle partitioning model (Pankow, 1994):

$$K_{\mathrm{org},i} = \frac{7.501RT}{10^9 \mathrm{MW}_{\mathrm{org}} \gamma_{\mathrm{org},i}\, p^o_{\mathrm{L},i}}, \quad (5)$$

$$K_{\mathrm{inorg},i} = \frac{7.501RT}{10^9 \mathrm{MW}_{\mathrm{inorg}} \gamma_{\mathrm{inorg},i}\, p^o_{\mathrm{L},i}}. \quad (6)$$

Here, R is the gas constant ($8.314\,\mathrm{J\,mol^{-1}\,K^{-1}}$) and T is temperature (K). $\mathrm{MW}_{\mathrm{org}}$ and $\mathrm{MW}_{\mathrm{inorg}}$ are the average molecular weights ($\mathrm{g\,mol^{-1}}$) of the organic and inorganic phases of the aerosol, respectively. $p^o_{\mathrm{L},i}$ is the subcooled liquid vapor pressure of a species, i. The activity coefficient in the org phase for each lumping species, $\gamma_{\mathrm{org},i}$, is assumed to be unity (Jang and Kamens, 1998). The activity coefficient in the inorg phase for each lumping species, $\gamma_{\mathrm{inorg},i}$, is predicted by a semiempirical regression equation that was fit to the activity coefficients of various organic compounds as a function of the physicochemical parameters (MW, O / C ratio, and HB) and sulfate fraction (FS). The FS is an indicator of aerosol acidity, which is defined as follows:

$$\mathrm{FS} = \frac{[\mathrm{SO_4^{2-}}]}{[\mathrm{SO_4^{2-}}] + [\mathrm{NH_4^+}]}, \quad (7)$$

where $[\mathrm{SO_4^{2-}}]$ and $[\mathrm{NH_4^+}]$ are the concentration of sulfate and ammonium ions, respectively. The semiempirical equation, derived from activity coefficients, estimated using the Aerosol Inorganic–Organic Mixtures Functional Groups Activity Coefficients (AIOMFAC) model (Zuend et al., 2011) at a given RH, is as follows:

$$\gamma_{\mathrm{inorg},i} = e^{0.035\cdot \mathrm{MW}_i - 2.704\cdot \ln(\mathrm{O}/\mathrm{C}_i) - 1.121\cdot \mathrm{HB}_i - 0.330\cdot \mathrm{FS} - 0.022\cdot(\cdot \mathrm{RH})}. \quad (8)$$

Further information on the derivation and statistical properties of Eq. (8) can be found in Zhou et al. (2019). The partitioning coefficients are used to calculate the concentration of each lumping species in the three phases ($C_{g,i}$, $C_{\mathrm{org},i}$, and $C_{\mathrm{inorg},i}$) from the total concentration of each lumping species ($C_{T,i}$). The total SOA mass formed by partitioning ($\mathrm{OM_P}$) in both the org and inorg phases is predicted by the following equation, which was developed by Schell et al. (2001) and reconstructed to consider mass formed by particle-phase reactions ($\mathrm{OM_{AR}}$), seen in Sect. 3.6, by Cao and Jang (2010):

$$\mathrm{OM_P} = \sum_i \left[C_{T,i} - \mathrm{OM}_{\mathrm{AR},i} - C^*_{g,i} \frac{\frac{C_{\mathrm{org},i}}{\mathrm{MW}_i}}{\sum_i \left(\frac{C_{\mathrm{org},i}}{\mathrm{MW}_i} + \frac{\mathrm{OM}_{\mathrm{AR},i}}{\mathrm{MW}_{\mathrm{oli},i}} \right) + \frac{\mathrm{OM}_0}{\mathrm{MW}_{\mathrm{oli},i}}} \right], \quad (9)$$

where C^*_g ($1/K_{\mathrm{org},i}$) and OM_0 ($\mathrm{mol\,m^{-3}}$) represent the effective saturation concentration and preexisting OM, respectively. $\mathrm{MW}_{\mathrm{oli},i}$ and MW_i represent the molecular weights of oligomeric products and lumping species, respectively. Equation (9) is solved using the Newton–Raphson method, which iterates until a convergence is reached (Press et al., 1992).

3.6 SOA formation by particle-phase reactions

$\mathrm{OM_{AR}}$ is formed in both the org and inorg phases. The inclusion of particle-phase reactions has been demonstrated to significantly improve predictions for aromatic hydrocarbons (Im et al., 2014; Zhou et al., 2019). Particle-phase reactions were also included in the study by Madhu et al. (2023) that demonstrated a negligible impact on linear-alkane SOA. In the org phase, SOA formation is attributed to oligomerization, as organic species undergo self-dimerization reactions (Han and Jang, 2020; Im et al., 2014; Yu et al., 2021b; Zhou et al., 2019). In the inorg phase, the oligomerization of organic species can be accelerated by an acid catalyst (Jang et al., 2002). Oligomerization is expressed as a second-order reaction (Odian, 2004) with rate constants $k_{\mathrm{AR,org},i}$ and $k_{\mathrm{AR,inorg},i}$ ($\mathrm{L\,mol^{-1}\,s^{-1}}$) in the org and inorg phases, respectively. $k_{\mathrm{AR,inorg},i}$ is described as follows:

$$k_{\mathrm{AR,inorg},i} = 10^{0.25\mathrm{pK}_{\mathrm{BH}^+_i} + 1.0X + 0.95R_i + \log(a_{\mathrm{w}}[H^+]) - 2.58}, \quad (10)$$

where R_i represents species reactivity, $\mathrm{pK}_{\mathrm{BH}^+ i}$ represents the protonation equilibrium constant, a_{w} represents the activity of water, X represents excess acidity (Cox and Yates, 1979), and $[H^+]$ represents the concentration of protons estimated using the extended aerosol inorganic model (E-AIM; Clegg et al., 1998). $k_{\mathrm{AR,org},i}$ is described as follows:

$$k_{\mathrm{AR,org},i} = 10^{[0.25\mathrm{pK}_{\mathrm{BH}^+_i} + 0.95R_i + 1.2\left(1 - \frac{1}{1+e^{0.005(300-\mathrm{MW}_{\mathrm{org}})}}\right) + \frac{2.2}{1+e^{6(0.75-\mathrm{O}/\mathrm{C})}} - 10.07]}. \quad (11)$$

For oligomerization in the org phase, the terms related to acidity (X and $a_w\left[H^+\right]$) are excluded. As explained by Zhou et al. (2019), a significant uncertainty remains in the calculation of $\left[H^+\right]$, specifically in low-RH and ammonia-rich environments, due to the poor performance of the E-AIM under these conditions (Li and Jang, 2012). Studies have previously demonstrated that aerosol viscosity can influence the mobility of chemical species and, thus, apparent reaction rates, which can be limited by slow bulk diffusion in the particle phase (De Schrijver and Smets, 1966; Reid et al., 2018). The molecular weight of species in the organic phase (MW_{org}) and the O / C ratio, which are important predictors of viscosity, are considered to calculate $k_{AR,org,i}$. Han and Jang (2022) demonstrate this method that accounts for viscosity in their application to SOA predictions from gasoline vapor composed of aromatic hydrocarbons and long-chain alkanes. Sulfuric acid can react with reactive organic compounds in the wet inorg phase of the aerosol to form dialkyl sulfate (diOS). The formed diOS can contribute to SOA mass production and leads to a reduction in $[H^+]$ which decreases the rate of SOA mass produced by acid-catalyzed oligomerization in the inorg phase. The formation of diOS is simulated in the UNIPAR model and reduces $[H^+]$ in the inorg phase, as previously reported (Im et al., 2014; Beardsley and Jang, 2016; Zhou et al., 2019).

3.7 Correction of intermediate organic vapor deposition to walls

Semi-volatile oxidized products derived from precursor HCs can deposit to chamber walls. As described in previous studies by Han and Jang (2020, 2022), the organic vapor deposition to the wall is kinetically treated at the given chamber with the deposition ($k_{on,i}$) and desorption ($k_{off,i}$) rate constants of each lumping species, i. $k_{on,i}$ is expressed as a fractional loss rate (McMurry and Grosjean, 1985):

$$k_{on,i} = \left(\frac{A}{V}\right)\frac{\alpha_{w,i}\overline{v}_i/4}{1+\frac{\pi\alpha_{w,i}\overline{v}_i}{8(K_eD)^{1/2}}}, \tag{12}$$

where D ($1.0\times10^{-6}\ m^2\ s^{-1}$) and K_e ($0.12\ s^{-1}$) are the diffusion coefficient and the coefficient of eddy diffusion applied as a fixed number, respectively. $\left(\frac{A}{V}\right)$ represents the surface-area-to-volume ratio of the chamber. $\overline{v}_i$ and $\alpha_{w,i}$ represent the mean thermal speed of the gas molecules and the accommodation coefficient of i to the wall, respectively. Further information regarding the calculation of $\overline{v}_i$ and $\alpha_{w,i}$ can be found a previous study (Madhu et al., 2023). $K_{w,i}$ ($K_{w,i} = k_{on,i}/k_{off,i}$) is calculated as follows:

$$\ln\left(K_{w,i}\right) = -\ln\left(\gamma_{w,i}\right) - \ln\left(p^o_{L,i}\right) + \ln\left(\frac{7.501RT\,OM_{wall}}{10^9 MW_{OM}}\right). \tag{13}$$

Here, OM_{wall} ($mg\ m^{-3}$) and MW_{OM} are the concentration of organic matter on the wall and the molecular weight of organic matter on the wall, respectively. The activity coefficient ($\gamma_{w,i}$) of lumping species, i, in OM_{wall} is calculated using the quantitative structure–activity relationship (QSAR) approach with the physicochemical properties $H_{d,i}$, $H_{a,i}$, and P_i, which represent hydrogen bond acidity, hydrogen bond basicity, and the polarizability of each lumping group i, respectively (Abraham et al., 1991; Abraham and McGowan, 1987; Leahy et al., 1992; Platts et al., 1999; Puzyn et al., 2010). Equation (13) can be rewritten as follows:

$$\ln\left(K_{w,i}\right) = -\left(a_pH_{d,i} + b_pH_{a,i} + r_pP_i + c_p\right) - \ln\left(p^o_{L,i}\right) + \ln\left(\frac{7.501RT\,OM_{wall}}{10^9 MW_{OM}}\right). \tag{14}$$

The values of $H_{d,i}$, $H_{a,i}$, and P_i are calculated with the PaDEL-Descriptor (Yap, 2011). The value of $K_{w,i}$ is used along with the $k_{on,i}$ to predict lumping species' wall loss using an analytical equation from the study by Han and Jang (2020) as follows:

$$C_{g,i} = \frac{K_{w,i}C_{T,i}}{K_{w,i}+1}e^{-k_{on,i}\left(1+\frac{1}{K_{w,i}}\right)t} + \frac{C_{T,i}}{K_{w,i}+1}, \tag{15}$$

where $C_{g,i}$ ($\mu g\ m^{-3}$) is the gas-phase concentration of a lumping species, i, after time step t (360 s). $C_{T,i}$ ($\mu g\ m^{-3}$) is the sum of $C_{g,i}$ and the concentration of lumping species i on the chamber wall ($C_{w,i}$, $\mu g\ m^{-3}$). This method for correcting the bias originating from gas–wall partitioning has been previously demonstrated for toluene, trimethylbenzene, α-pinene (Hang and Jang, 2020), and linear alkanes (Madhu et al., 2023), as well as a composition of gasoline vapor (Han and Jang, 2022). As explained by Hang and Jang (2020), uncertainties in this method are associated with the calculation of physicochemical parameters of lumped groups. The properties of gas–wall partitioning for branched alkanes were inherited from linear alkanes.

3.8 UNIPAR procedure for SOA mass production at each time step

At each step, $C_{T,i}$ is estimated using the newly produced ΔHC and α_i, and it is combined with the previous step's concentration of lumping species, except those used for the formation of OM_{AR} and organic vapor deposition to walls for the simulation of chamber data. Then, the updated $C_{T,i}$ is applied to generate $C_{g,i}$, $C_{org,i}$, and $C_{inorg,i}$ based on multiphase partitioning coefficients, as seen in Eqs. (5) and (6). C_{inorg} and C_{org} are then used to form OM_{AR} via oligomerization in both the inorg and org phases with the rate constants calculated in Eqs. (10) and (11), respectively. In the model, the quantity of the sulfate associated with OS in the inorg phase is also estimated and applied to recalculate $[H^+]$. After the process to form OM_{AR}, the remaining concentration of lumping species is used to estimate the organic vapor deposition to the wall using Eq. (15). OM_P is calculated using a Newtonian approach (Eq. 9) in the presence of OM_{AR} and

the preexisting OM_0 at the end of each time step. For the total SOA mass, OM_{AR}, OM_P, and OM_0 are combined.

4 Results and discussion

4.1 Chamber data vs. model prediction

The feasibility of the UNIPAR model to predict SOA formation from various branched alkanes (Table S1) was demonstrated by comparing simulations with chamber data collected under various experimental conditions in the UF-APHOR chamber. As seen in Fig. 2, the UNIPAR model is reasonably able to predict SOA formation from 2,6,10-trimethyldodecane (C15), 2,2,4,4,6,8,8-heptamethylnonane (C16), and 2,6,10,14-tetramethylpentadecane (C19) at both high- and low-NO_x conditions under different seed conditions (Table 1). Gas simulations used to predict HC consumption, RO_2 concentrations, and HO_2 concentrations performed using the CB6 mechanism can be seen in Fig. S3. As seen in the gas simulation, the consumption of isododecane was overpredicted compared with chamber measurements. This is likely due to the relatively low purity (80 %) of the commercially available isododecane that was used for the chamber experiment. However, even with an overprediction for the gas consumption, the UNIPAR model SOA showed only a slight overprediction, indicating that the relatively low SOA yield of isododecane is well represented within the model.

Generally, the presence of branching significantly reduced the amount of alkane SOA mass. This impact can be seen when comparing chamber data generated for isododecane (branched C12) to linear C12 and chamber data generated for trimethyldodecane (branched C15) to linear C15, as visible in Fig. 3. Remarkably, highly branched C16 (Fig. 2) shows a lower capability for SOA formation compared with linear C15 (Fig. 3). Overall, the typical impact of NO_x levels on SOA formation appeared, showing a negative relationship. Unlike SOA generated from aromatics (Im et al., 2014), branched-alkane SOA was insensitive to the seed condition due to the low polarity of the products. A similar result is observed in linear-alkane SOA reported by Madhu et al. (2023). Further discussion on the impact of alkyl branches, NO_x conditions, humidity, seed, and temperature can be found in the following (Sect. 4.3 and 4.4).

4.2 Characterization of aerosol composition

Figure 4 displays the relative functional group compositions of various alkane SOA constructed using FTIR data. FTIR spectra were decoupled into functional groups using the curve-fitting method, assuming that a Gaussian distribution governs each peak. The decoupled FTIR bend for each functional group was applied to estimate the functional group composition of alkane aerosol using the relative intensity of the functional group determined from various reference compounds. The fitting parameters are the center frequency, the peak absorbance, and the half-width at half-height. The relative functional group intensities for −OH, −COOH, C=O in ketones and aldehydes, C−O in non-alcohol and non-carboxylic acid groups, and NO_3 in organonitrates were normalized with that of C–H stretching. The O / C ratios, calculated using functional group distributions from FTIR spectra, are also shown in Fig. 4 alongside model-predicted O / C ratios. Values for peak ranges for each functional group and oxygen and carbon content values used to calculate O / C ratios can be found in Table S5. The model is able to reasonably predict O / C ratios for chamber-generated data for both branched and linear alkanes. As expected, alkanes with a larger number of carbons tend to produce less-oxidized SOA compared with alkanes with a smaller number of carbons. The relatively low O / C ratios found in alkane SOA systems support our assumption that organic and wet inorganic phases exist separately, as most organic species are unlikely to be soluble in the inorganic phase (Yu et al., 2021a). When comparing the SA-seeded C19 and non-seeded C19 SOA systems, the SA system shows smaller number of C=O functional groups but a higher number of C–O groups, evidently indicating some acid-catalyzed oligomerization (Jang et al., 2002), although the impact of wet inorganic seed is small (Sect. 4.4). All SOA systems shown in Fig. 4 are produced under relatively low NO_x conditions (Table 1). Increasing the NO_x levels during alkane oxidation may increase the presence of nitrate functional groups in SOA.

4.3 Sensitivity of alkane SOA yields to alkyl branches

Figure 5 illustrates the impact of alkyl branches on the SOA yields of an alkane with 15 carbons. Information on the structures, parameters used to generate lumping arrays, and calculated OH-radical reaction rates for alkanes used in Fig. 5 can be found in Table S5. Figure 5 clearly demonstrates a decrease in alkane SOA yields as the number of alkyl branches increases under given oxidation conditions. This result qualitatively agrees with previous literature that explores the impact of alkyl branches on the SOA yields of alkanes (Loza et al., 2014; Lim and Ziemann, 2009; Tkacik et al., 2012). This figure also illustrates the relative importance of the ARF in the model compared to the vapor pressure drop due to branching. When the number of branches increases, the decrease in vapor pressure may not be large enough such that the linear alkane with the nearest vapor pressure changes. For example, C15 alkanes with one branch and two branches, at the given structures, both have vapor pressures nearest to that of linear C14 (Table S5). In this case, the ARF becomes the only method to decrease SOA yields, and the decrease in SOA yields due to an increase in alkyl branches is relatively small within the model. This suggests that the primary driver in the reduction in the alkane SOA yields due to branching is the increase in vapor pressure, with the ARF being a significantly smaller component. Additionally, when comparing the C15 alkane with one branch to the one with

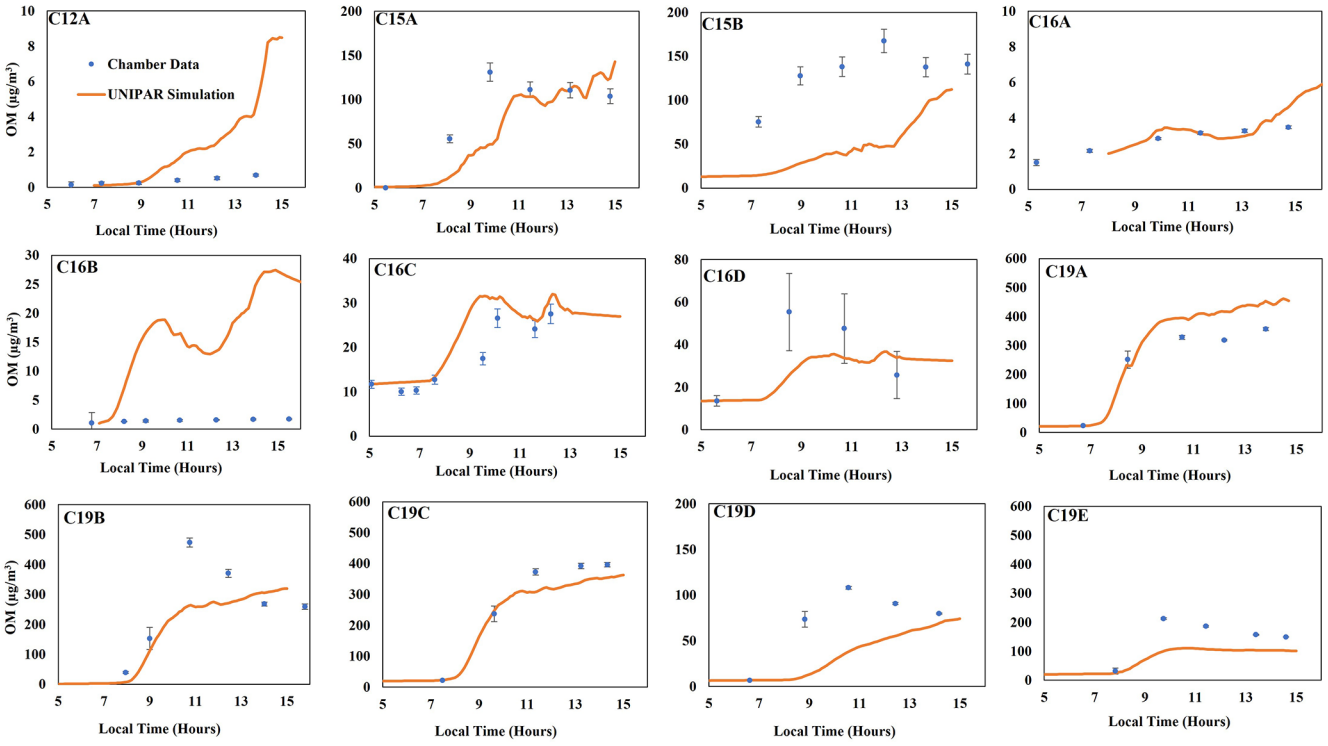

Figure 2. Comparison of SOA mass produced between simulations for isododecane, trimethyldodecane, heptamethylnonane, and tetramethylpentadecane to chamber data (Table 1). The blue dots represent observed SOA data collected that have been corrected for particle wall loss to the chamber. Error bars represent a 95 % confidence interval for each data point.

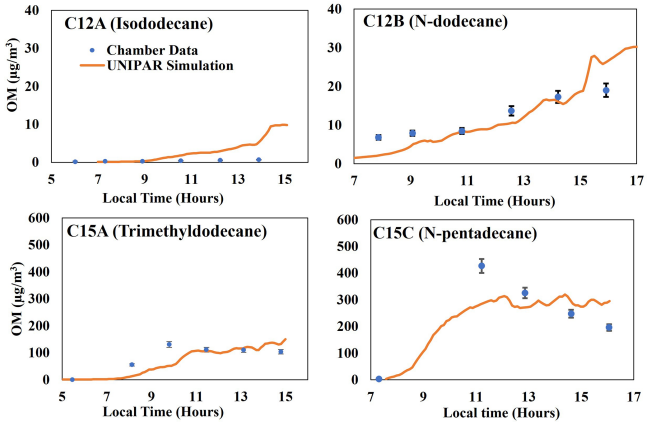

Figure 3. Comparison of the SOA mass produced by two-branched alkanes (isododecane and trimethyldodecane) to the mass produced by linear alkanes (Madhu et al., 2023) of the same carbon number (Table 1). Error bars for C12A and C15A represent a 95 % confidence interval for each data point. Error bars for C12B and C15C are 8 %, as reported by Madhu et al. (2023).

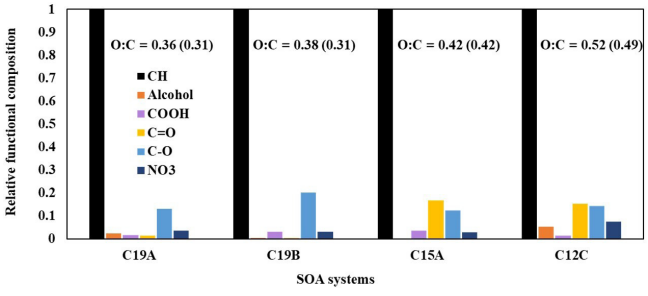

Figure 4. Relative functional group compositions of different SOA systems constructed using FTIR data. The O / C ratios of each SOA system, constructed with the functional group composition from FTIR data, are shown along with model-predicted O / C ratios displayed in parentheses.

two branches, the difference in SOA yields for the low-NO_x condition is slightly larger when compared with the difference in SOA yields for the high-NO_x condition. This indicates that, similarly to linear alkanes (Madhu et al., 2023), the fraction of branched-alkane autoxidation products of total SOA mass under low-NO_x conditions is larger compared with that under high-NO_x conditions. Further discussion on the impact of NO_x conditions on the SOA yields of branched alkanes can be found in Sect. 4.4.

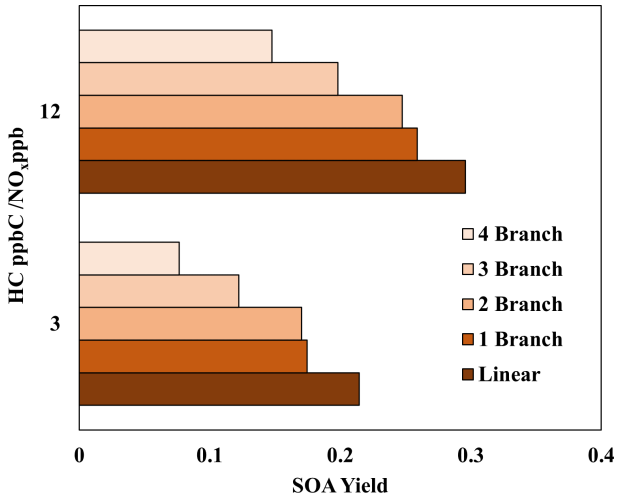

Figure 5. Simulated SOA yields for 15-carbon alkanes with various number of branches at two different NO_x levels. $OM_0 = 5\,\mu g\,m^{-3}$, 298 K, RH = 60 %, HC consumption = $100\,\mu g\,m^{-3}$, and the sunlight profile is shown in Fig. S4.

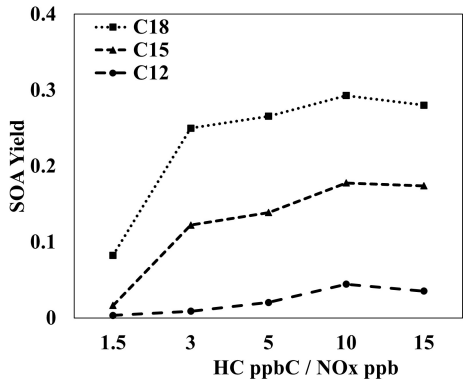

Figure 6. Simulated SOA yields for three-branched alkanes of different carbon numbers (C12, C15, C18) at various HC ppbC / NO_x ppb levels. $OM_0 = 5\,\mu g\,m^{-3}$, 298 K, RH = 60 %, HC consumption = $100\,\mu g\,m^{-3}$, and the sunlight profile is shown in Fig. S4.

4.4 Sensitivity of branched-alkane SOA formation to NO_x levels, temperature, humidity, and seed conditions

Figure 6 illustrates the SOA yields of three alkanes that each have three branched-methyl groups (C12, C15, C18) under various NO_x levels. Information on the structures, parameters used to generate lumping arrays, and calculated OH-radical reaction rates for alkanes used in Fig. 6 can be found in Table S6. Similarly to most SOA precursors, the simulated SOA yields of all three branched alkanes increased as NO_x levels decreased. Because gas simulations are conducted in a manner via which the HC consumption is kept fixed for each condition, the difference between SOA yields at different NO_x levels can be attributed to a change in product distributions. Under high-NO_x conditions, the paths to form organonitrate products can compete with the paths that form low-volatility products via autoxidation. In addition, the formation of organonitrate suppresses the further oxidation of products. Less-oxidized products tend to be more volatile products, reducing SOA yields. This result is in agreement with Loza et al. (2014), who found a higher yield for isododecane under low-NO_x conditions when similar amounts of hydrocarbon were consumed under both high- and low-NO_x conditions.

Figure 7 illustrates the SOA yields of 2,6,10-trimethyldodecane under three different seed conditions (ammonium sulfate, AS; sulfuric acid, SA; and no seed, NS) and two RH conditions (30 % and 60 %). Under 60 % RH, the AS seed is wet, whereas the AS seed is dry under 30 % RH. Similarly to linear alkanes (Madhu et al., 2023), branched-alkane SOA yields were not significantly impacted by the presence of seed under either humidity condition. Additionally, no significant impact of acidic seed on branched alkanes appeared, indicating that alkane SOA formation is dominated by partitioning rather than particle-phase chemistry. This is consistent with the FTIR data (Fig. 4) that show a lack of reactive aldehydic C=O species which can be involved in acid-catalyzed oligomerization.

Figure 8 displays the SOA yields of three different three-branched alkanes (Table S6) under three different temperatures and two different NO_x conditions. As expected, due to the relatively high importance of partitioning, the SOA yields of all the three-branched alkanes are significantly impacted by changes in temperature under both NO_x conditions. Additionally, the impact of temperature on SOA yields decreases as the number of carbons increases, as larger molecules typically produce more low-volatility products which tend to exist in the particle-phase at various temperatures.

4.5 Uncertainty of model rate constants

Figure 9 illustrates the impact of increasing and decreasing the UNIPAR oligomerization rate constant by a factor of 2 on the SOA yields of 2,6,10-trimethyldodecane at both high and low NO_x levels. Unlike aromatic SOA (Im et al., 2014; Zhou et al., 2019; Han and Jang, 2022), the SOA yields were not significantly impacted by either change to the oligomerization rate constant under both NO_x conditions. This reaffirms the previously discussed (Sect. 4.2, 4.4) idea that particle-phase reactions (oligomerization reactions) play a relatively small role in branched-alkane SOA formation due to the lack of reactive oxidation products. Thus, within this model, there is a low level of uncertainty which originates from the rate constant for particle-phase reactions.

Vapor pressures related to volatility groups were calculated using a group contribution method that has an estimated uncertainty of a factor of 1.45 (Zhao et al., 1999; Myrdal and Yalkowsky, 1997). Figure 10 displays the impact of uncertainties in the estimation of vapor pressure in UNIPAR.

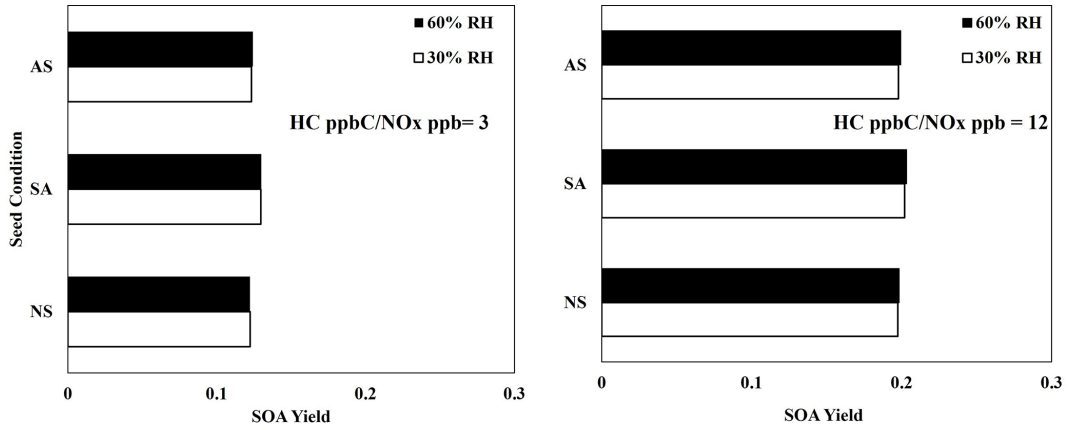

Figure 7. Simulated SOA yields for 2,6,10-trimethyldodecane at various seed conditions, 10 µg m^{-3} ammonium sulfate (AS), 10 µg m^{-3} sulfuric acid (SA), and no seed (NS), and two HC ppbC / NO_x ppb levels. $OM_0 = 5$ µg m^{-3}, 298 K, RH = 60 %, HC consumption = 100 µg m^{-3}, and the sunlight profile is shown in Fig. S4.

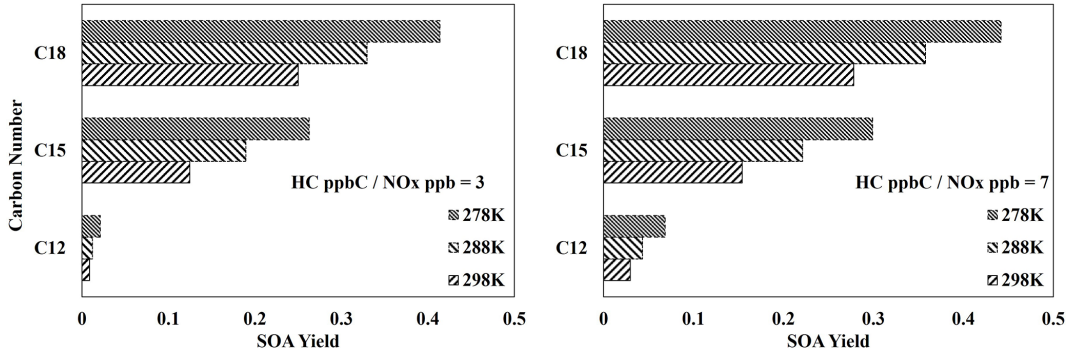

Figure 8. Simulated SOA yields from the photooxidation of three different three-branched alkanes (Table S3) at three different temperatures (278, 288, 298 K) and two different NO_x levels (HC ppbC / NO_x ppb = 3, 7). $OM_0 = 5$ µg m^{-3}, RH = 60 %, HC consumption = 100 µg m^{-3}, and the sunlight profile is shown in Fig. S4.

Contrary to the oligomerization rate constant, changing the lumping group vapor pressures causes significant changes in SOA yield, demonstrating the important role of partitioning in branched-alkane SOA formation.

4.6 Application of IVC-based product distributions to SOA simulation from diesel linear and branched alkanes

Diesel fuel is comprised of various linear and branched alkanes that dominantly range from C9 to C24. The composition of linear and branched alkanes in diesel fuel, reported by Gentner et al. (2012), was applied to the UNIPAR model, as shown in Fig. 11. The gas simulation of diesel fuel was performed using the CB6 ozone mechanism with relative concentrations of diesel fuel linear and branched alkanes (100 µg m^{-3} total), as well as other common diesel constituents, as reported by Sazhin et al. (2014), under urban conditions (high NO_x level). SOA formation was simulated only from branched and linear alkanes, but the inclusion other diesel constituents allows for more accurate predictions of concentrations RO_2 and HO_2, as well as individual HC consumptions. It is important to note that the composition of branched and linear alkanes in fuels will vary from the composition of those in fuel exhausts. However, literature that reports the composition of fuel exhaust typically provides significant proportions of branched alkanes as unspeciated branched alkanes (Lu et al., 2018; Tkacik et al., 2014). Thus, current diesel exhaust compositions cannot be used for this analysis. Each branched alkane was assumed to have three methyl branches. Within the UNIPAR model, SOA formation from all linear and branched alkanes was performed simultaneously, such that the SOA mass formed from one precursor can enhance the SOA mass formed from every other precursor. As seen in Fig. 11, branched alkanes represent a higher proportion of diesel fuel and also of SOA mass formed compared with linear alkanes. Branched alkanes represented 78 % of the alkane HC input and were responsible for 72 % of the total SOA mass produced.

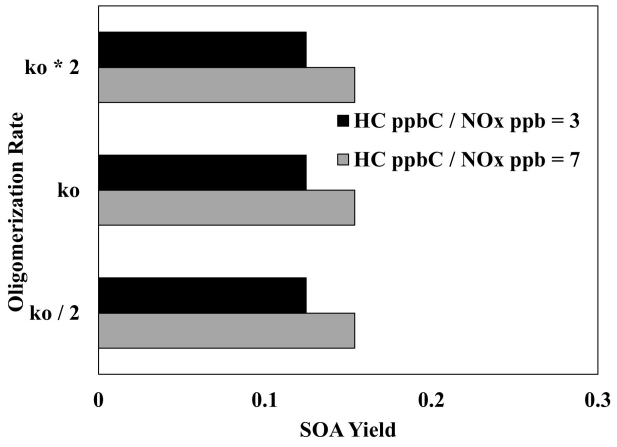

Figure 9. Impact of increasing and decreasing the UNIPAR oligomerization rate constant by a factor of 2 on the SOA yields of 2,6,10-trimethyldodecane at two different NO_x levels (HC ppbC / NO_x ppb = 3, 7). $OM_0 = 5\,\mu g\,m^{-3}$, RH = 60 %, HC consumption = $100\,\mu g\,m^{-3}$, and the sunlight profile is shown in Fig. S4.

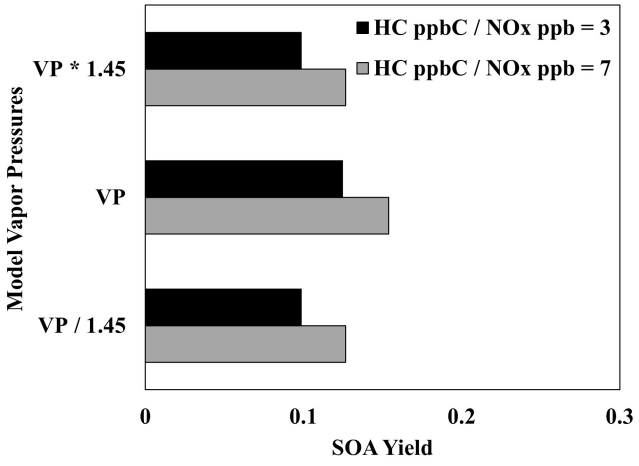

Figure 10. Impact of increasing and decreasing the UNIPAR lumping group vapor pressures by a factor of 1.45 on the SOA yields of 2,6,10-trimethyldodecane at two different NO_x levels (HC ppbC / NO_x ppb = 3, 7). $OM_0 = 5\,\mu g\,m^{-3}$, RH = 60 %, HC consumption = $100\,\mu g\,m^{-3}$, and the sunlight profile is shown in Fig. S4.

Additionally, long-chain alkanes ($\geq$ C15) are relatively more important for SOA formation compared with smaller alkanes within both the linear and branched subsets. Long-chain linear alkanes represented 59 % of the linear-alkane composition in diesel and were responsible for 73 % of the total linear-alkane SOA mass production. Similarly, long-chain branched alkanes represented 56 % of the branched-alkane composition in diesel fuel and were responsible for 75 % of the total branched-alkane SOA mass production. Our conclusion regarding the importance of long-chain alkanes generally agrees with the conclusion presented by Madhu et al. (2023). However, the linear-alkane SOA formation simulation by Madhu et al. (2023) was performed individually for each precursor, which did not allow for SOA mass produced from one precursor to influence the others. Thus, Fig. 11 is a better representation of the SOA formation potential from linear and branched alkanes in diesel fuel. However, the inclusion of other diesel constituents (e.g., cyclic alkanes, polyaromatics HCs, and aromatics) may further augment the SOA formation potential of the various linear and branched alkanes' diesel fuel (Gentner et al., 2012).

4.7 Summary and conclusions

Branched alkanes are one of the major classes of HCs in urban environments, specifically representing significant proportions of both gasoline and diesel fuel (Gentner et al., 2012). This study models SOA formation using the UNIPAR model via the multiphase reactions of branched alkanes. Due to a lack of practically applicable gas mechanisms available for a variety of branched alkanes, the lumping arrays of branched alkanes were predicted using previously existing lumping arrays of linear alkanes. To do so, the lumping array of each branched alkane was primarily created using the lumping array of the linear alkane with the nearest vapor pressure. In addition to a decrease in vapor pressure, branching present on an alkane chain can reduce the ability of the oxidation products to undergo autoxidation (Fig. S2). Autoxidation has been demonstrated in previous studies which show that autoxidation products significantly contribute to terpene SOA (Pye et al., 2019; Xavier et al., 2019; Yu et al., 2021b) and linear-alkane SOA (Madhu et al., 2023). To account for the reduction of autoxidation products in branched alkanes compared with that in linear alkanes, an ARF value (Eq. 4) was applied to the α values of lumping groups. Lumping arrays generated in this manner were applied within UNIPAR to predict SOA formation from branched alkanes, which was compared to chamber data. Notably, the presence of alkyl branches can also significantly increase the number of decomposition reactions that produce more volatile products (Loza et al., 2014; Lim and Ziemann, 2009; Tkacik et al., 2012). Whereas the increase in decomposition reactions due to alkyl branches is not explicitly accounted for, our application of the ARF implicitly captures some increase in decomposition. We apply the ARF to reduce the value of the stoichiometric coefficient related to the lumped groups which yield autoxidation products. The amount of the stoichiometric coefficient that is expelled from the α_i array via this reduction is essentially treated as products that are so highly volatile that they cannot form SOA via gas–particle partitioning. The model-predicted SOA formation agreed well with chamber data (Fig. 2). Additionally, O / C values of chamber-generated SOA, which were calculated using FTIR spectra, were also in agreement with model-predicted O / C values. Similarly to linear alkanes (Madhu et al., 2023), branched alkanes showed significant sensitivity to

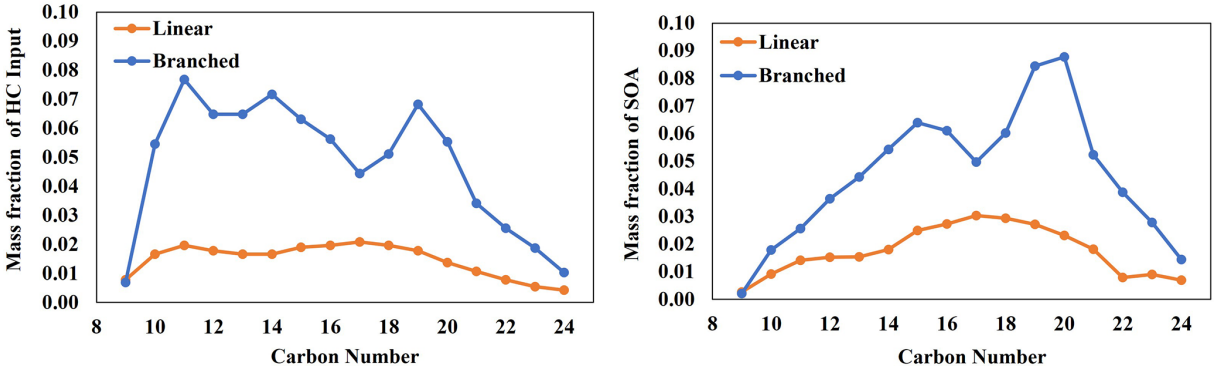

Figure 11. SOA formation from the photooxidation of diesel fuel linear and branched alkanes in the presence of NO_x. Composition is as reported by Gentner et al. (2012). Concentration of initial HC = 993 ppbC, temperature = 298 K, RH = 60 %, HC ppbC / NO_x ppb = 3, and the sunlight profile is shown in Fig. S4.

NO_x levels, as seen in Fig. 6. The degree of branching was also shown to significantly impact branched-alkane SOA, with yields generally decreasing as the number of methyl branches increased (Fig. 5). As branching increased, the vapor pressure increase in the precursor and subsequent oxidation products was determined to be a more significant factor contributing to branched-alkane SOA yields than the ARF (Sect. 4.3). The branched-alkane SOA formation is dominated by gas–particle partitioning processes, particularly between the gas and organic phases due to the relatively nonpolar, nonreactive oxidation products. Evidently, SOA yields are sensitive to temperature (Fig. 8), an environmental factor that is heavily tied to partitioning. Furthermore, branched-alkane SOA yields are insensitive to changes in particle-phase reaction rates (Fig. 9) and show no significant impacts from changes in aerosol acidity or inorganic seed composition (Fig. 7).

The conclusions presented have several real-world implications. Firstly, branched alkanes are significant sources of SOA formation and should be considered as an SOA precursor, especially in urban environments where vehicular emissions represent a significant proportion of the emitted reactive organic carbon (Murphy et al., 2023). As shown in Fig. 11, branched alkanes within diesel were responsible for a significantly larger proportion of SOA mass production compared with linear alkanes. Secondly, the reduction in the NO_x concentrations in the atmosphere would not be effective to decrease branched-alkane SOA formation, as branched-alkane SOA yields tend to increase as NO_x levels decrease (Fig. 6). Thirdly, branched-alkane SOA yields would not be significantly affected by the reduction in sulfate because of relatively nonpolar, nonreactive oxidative products (Sect. 4.4). Notably, the chamber experiments that are used to validate the model results occur at half-day timescales. Further atmospheric aging could change oxidation product compositions and alter SOA mass yields. Additionally, compounds used in this study, which were picked from a limited set of commercially available branched alkanes, are generally larger and less branched compared with those identified in the atmosphere and in fuel exhausts. However, even in the case that the atmosphere contains significant amounts of small, highly branched compounds, those would be less relevant for SOA formation potential than the compounds used in this study due to negligible SOA yields. Branched-alkane SOA predictions using the UNIPAR model contain several sources of uncertainty. As previously explained, the UNIPAR parameters of each branched alkane were primarily inherited from an analogous linear alkane. For example, vapor pressures of precursor branched alkanes were matched with the linear alkane with the nearest vapor pressure. However, the two matched vapor pressures are rarely identical, and this deviation between the two values can yield uncertainty in the predicted lumping array. Similarly, physicochemical parameters (e.g., O / C, HB, and MW arrays as well as wall loss parameters) inherited from linear alkanes can be included as sources of uncertainty in SOA prediction. Additionally, the branched-alkane lumping arrays also inherited uncertainty associated with the linear-alkane oxidation mechanisms that were originally used to generated linear-alkane lumping arrays. As described by Madhu et al. (2023), the linear-alkane gas oxidation mechanisms used to generate lumping arrays were written in such a way that if a precursor has several possible points of reaction with a hydroxyl radical, only one path is included. The inclusion of alternative pathways may augment the linear-alkane lumping arrays and have downstream effects on branched-alkane lumping arrays. Uncertainties also exist in hydrocarbon consumption values simulated by CB6. As described in Sect. S1, the CB6 model overpredicts hydroxyl radical concentrations for chamber experiments performed with long-chain alkanes. Accordingly, gas simulations had a tendency toward the overprediction of hydrocarbon consumption. In this study, SOA formation from the photooxidation of linear and branched alkanes in diesel fuel was predicted using the UNIPAR model. How-

ever, diesel fuels also contain significant amounts of cyclic alkanes, which tend to have higher propensities to be SOA precursors (Manavi and Pandis, 2022; Loza et al., 2014; Lim and Ziemann, 2009). When considering SOA formation from alkanes in diesel, future studies should include cyclic alkanes to accurately predict SOA formation potentials.

Code availability. The code to run the UNIPAR model in this study is available upon reasonable request. UNIPAR is freely available to the public via Zenodo https://doi.org/10.5281/zenodo.11151155 (Madhu et al., 2024).

Data availability. Chamber data and model simulations for the branched-alkane experiments performed in this study are publicly available on Zenodo (https://zenodo.org/records/10667797, Madhu and Jang, 2024).

Supplement. The supplement related to this article is available online at: https://doi.org/10.5194/acp-24-5585-2024-supplement.

Author contributions. MJ designed the experiments and AM and MJ carried them out. Model parameters were developed by MJ and AM. Model simulations were performed by AM. Model sensitivity testing was designed by AM, MJ, and YJ and performed by AM. AM prepared the manuscript with edits from MJ.

Competing interests. The contact author has declared that none of the authors has any competing interests.

Disclaimer. Publisher's note: Copernicus Publications remains neutral with regard to jurisdictional claims made in the text, published maps, institutional affiliations, or any other geographical representation in this paper. While Copernicus Publications makes every effort to include appropriate place names, the final responsibility lies with the authors.

Financial support. This research has been supported by the National Institute of Environmental Research (grant no. NIER2021), the National Science Foundation (grant no. AGS1923651), and the National Research Foundation of Korea (grant no. 2020M3G1A1114556).

Review statement. This paper was edited by Allan Bertram and reviewed by two anonymous referees.

References

Abraham, M. H. and McGowan, J. C.: The Use of Characteristic Volumes to Measure Cavity Terms in Reversed Phase Liquid Chromatography, Chromatographia, 23, 243–246, 1987.

Abraham, M. H., Whiting, G. S., Doherty, R. M., and Shuely, W. J.: Hydrogen bonding: XVI. A new solute salvation parameter, π_2^H, from gas chromatographic data, J. Chromatogr. A, 587, 213–228, https://doi.org/10.1016/0021-9673(91)85158-C, 1991.

Alves, C., Vicente, A., Pio, C., Kiss, G., Hoffer, A., Decesari, S., Prevôt, A. S. H., Minguillón, M. C., Querol, X., Hillamo, R., Spindler, G., and Swietlicki, E.: Organic compounds in aerosols from selected European sites – Biogenic versus anthropogenic sources, Atmos. Environ., 59, 243–255, https://doi.org/10.1016/j.atmosenv.2012.06.013, 2012.

Aumont, B., Camredon, M., Mouchel-Vallon, C., La, S., Ouzebidour, F., Valorso, R., Lee-Taylor, J., and Madronich, S.: Modeling the influence of alkane molecular structure on secondary organic aerosol formation, Roy. Soc. Ch., 165, 105–122, 2013.

Beardsley, R. L. and Jang, M.: Simulating the SOA formation of isoprene from partitioning and aerosol phase reactions in the presence of inorganics, Atmos. Chem. Phys., 16, 5993–6009, https://doi.org/10.5194/acp-16-5993-2016, 2016.

Bianchi, F., Kurtén, T., Riva, M., Mohr, C., Rissanen, M. P., Roldin, P., Berndt, T., Crounse, J. D., Wennberg, P. O., Mentel, T. F., Wildt, J., Junninen, H., Jokinen, T., Kulmala, M., Worsnop, D. R., Thornton, J. A., Donahue, N., Kjaergaard, H. G., and Ehn, M.: Highly Oxygenated Organic Molecules (HOM) from Gas-Phase Autoxidation Involving Peroxy Radicals: A Key Contributor to Atmospheric Aerosol, Chem. Rev., 119, 3472–3509, https://doi.org/10.1021/acs.chemrev.8b00395, 2019.

Cao, G. and Jang, M.: An SOA Model for Toluene Oxidation in the Presence of Inorganic Aerosols, Environ. Sci. Technol., 44, 727–733, https://doi.org/10.1021/es901682r, 2010.

Caplain, I., Cazier, F., Nouali, H., Mercier, A., Déchaux, J.-C., Nollet, V., Joumard, R., André, J.-M., and Vidon, R.: Emissions of unregulated pollutants from European gasoline and diesel passenger cars, Atmos. Environ., 40, 5954–5966, https://doi.org/10.1016/j.atmosenv.2005.12.049, 2006.

Choi, J. and Jang, M.: Suppression of the phenolic SOA formation in the presence of electrolytic inorganic seed, Sci. Total Environ., 851, 158082, https://doi.org/10.1016/j.scitotenv.2022.158082, 2022.

Clegg, S. L., Brimblecombe, P., and Wexler, A. S.: Thermodynamic Model of the System H^+-NH_4^+-SO_4^{2-}–NO_3^--H_2O at Tropospheric Temperatures, J. Phys. Chem. A, 102, 2137–2154, https://doi.org/10.1021/jp973042r, 1998.

Cox, R. A. and Yates, K.: Kinetic equations for reactions in concentrated aqueous acids based on the concept of "excess acidity", Can. J. Chem., 57, 2944–2951, https://doi.org/10.1139/v79-479, 1979.

Crounse, J. D., Nielsen, L. B., Jørgensen, S., Kjaergaard, H. G., and Wennberg, P. O.: Autoxidation of Organic Compounds in the Atmosphere, J. Phys. Chem. Lett., 4, 3513–3520, https://doi.org/10.1021/jz4019207, 2013.

De Schrijver, F. and Smets, G.: Polymerization kinetics in highly viscous media, J. Poly. Sci. A1, 4, 2201–2210, https://doi.org/10.1002/pol.1966.150040914, 1966.

Emery, C., Jung, J., Koo, B., and Yarwood, G.: Improvements to CAMx Snow Cover Treatments and Carbon Bond Chemical Mechanism for Winter Ozone, http://www.camx.com/files/udaq_snowchem_final_6aug15.pdf (last access: 10 February 2024), 2015.

Emmerson, K. M. and Evans, M. J.: Comparison of tropospheric gas-phase chemistry schemes for use within global models, Atmos. Chem. Phys., 9, 1831–1845, https://doi.org/10.5194/acp-9-1831-2009, 2009.

Finlayson-Pitts, B. J. and Pitts, J. N.: CHAPTER 4 – Photochemistry of Important Atmospheric Species, in: Chemistry of the Upper and Lower Atmosphere, edited by: Finlayson-Pitts, B. J., and Pitts, J. N., Academic Press, San Diego, 86–129, https://doi.org/10.1016/B978-012257060-5/50006-X, 2000.

Gentner, R., Isaacman, G., Worton David, R., Chan Arthur, W. H., Dallmann Timothy, R., Davis, L., Liu, S., Day Douglas, A., Russell Lynn, M., Wilson Kevin, R., Weber, R., Guha, A., Harley Robert, A., and Goldstein Allen, H.: Elucidating secondary organic aerosol from diesel and gasoline vehicles through detailed characterization of organic carbon emissions, P. Natl. Acad. Sci. USA, 109, 18318–18323, https://doi.org/10.1073/pnas.1212272109, 2012.

Han, S. and Jang, M.: Simulating the impact of gas-wall partitioning on SOA formation using the explicit gas mechanism integrated with aqueous reactions containing electrolytes, Sci. Total Environ., 748, 141360, https://doi.org/10.1016/j.scitotenv.2020.141360, 2020.

Han, S. and Jang, M.: Prediction of secondary organic aerosol from the multiphase reaction of gasoline vapor by using volatility–reactivity base lumping, Atmos. Chem. Phys., 22, 625–639, https://doi.org/10.5194/acp-22-625-2022, 2022.

Im, Y., Jang, M., and Beardsley, R. L.: Simulation of aromatic SOA formation using the lumping model integrated with explicit gas-phase kinetic mechanisms and aerosol-phase reactions, Atmos. Chem. Phys., 14, 4013–4027, https://doi.org/10.5194/acp-14-4013-2014, 2014.

Jang, M. and Kamens, R. M.: A Thermodynamic Approach for Modeling Partitioning of Semivolatile Organic Compounds on Atmospheric Particulate Matter: Humidity Effects, Environ. Sci. Technol., 32, 1237–1243, https://doi.org/10.1021/es970773w, 1998.

Jang, M., Czoschke, N. M., Lee, S., and Kamens, R. M.: Heterogeneous Atmospheric Aerosol Production by Acid-Catalyzed Particle-Phase Reactions, Science, 298, 814–817, https://doi.org/10.1126/science.1075798, 2002.

Jo, Y., Jang, M., Han, S., Madhu, A., Koo, B., Jia, Y., Yu, Z., Kim, S., and Park, J.: CAMx–UNIPAR simulation of secondary organic aerosol mass formed from multiphase reactions of hydrocarbons under the Central Valley urban atmospheres of California, Atmos. Chem. Phys., 24, 487–508, https://doi.org/10.5194/acp-24-487-2024, 2024.

La, Y. S., Camredon, M., Ziemann, P. J., Valorso, R., Matsunaga, A., Lannuque, V., Lee-Taylor, J., Hodzic, A., Madronich, S., and Aumont, B.: Impact of chamber wall loss of gaseous organic compounds on secondary organic aerosol formation: explicit modeling of SOA formation from alkane and alkene oxidation, Atmos. Chem. Phys., 16, 1417–1431, https://doi.org/10.5194/acp-16-1417-2016, 2016.

Leahy, D. E., Morris, J. J., Taylor, P. J., and Wait, A. R.: Model solvent systems for QSAR. Part 3. An LSER analysis of the "critical quartet." New light on hydrogen bond strength and directionality, J. Chem. Soc. Perk. T. 2, 705–722, https://doi.org/10.1039/p29920000705, 1992.

Li, J. and Jang, M.: Aerosol Acidity Measurement Using Colorimetry Coupled With a Reflectance UV-Visible Spectrometer, Aerosol Sci. Tech., 46, 833–842, https://doi.org/10.1080/02786826.2012.669873, 2012.

Li, J., Wang, W., Li, K., Zhang, W., Peng, C., Zhou, L., Shi, B., Chen, Y., Liu, M., Li, H., and Ge, M.: Temperature effects on optical properties and chemical composition of secondary organic aerosol derived from n-dodecane, Atmos. Chem. Phys., 20, 8123–8137, https://doi.org/10.5194/acp-20-8123-2020, 2020.

Li, J., Li, K., Li, H., Wang, X., Wang, W., Wang, K., and Ge, M.: Long-chain alkanes in the atmosphere: A review, J. Environ. Sci., 114, 37–52, https://doi.org/10.1016/j.jes.2021.07.021, 2022.

Lim, Y. B. and Ziemann, P. J.: Effects of Molecular Structure on Aerosol Yields from OH Radical-Initiated Reactions of Linear, Branched, and Cyclic Alkanes in the Presence of NO_x, Environ. Sci. Technol., 43, 2328–2334, https://doi.org/10.1021/es803389s, 2009.

Loza, C. L., Craven, J. S., Yee, L. D., Coggon, M. M., Schwantes, R. H., Shiraiwa, M., Zhang, X., Schilling, K. A., Ng, N. L., Canagaratna, M. R., Ziemann, P. J., Flagan, R. C., and Seinfeld, J. H.: Secondary organic aerosol yields of 12-carbon alkanes, Atmos. Chem. Phys., 14, 1423–1439, https://doi.org/10.5194/acp-14-1423-2014, 2014.

Lu, Q., Zhao, Y., and Robinson, A. L.: Comprehensive organic emission profiles for gasoline, diesel, and gas-turbine engines including intermediate and semi-volatile organic compound emissions, Atmos. Chem. Phys., 18, 17637–17654, https://doi.org/10.5194/acp-18-17637-2018, 2018.

Lyu, Y., Xu, T., Yang, X., Chen, J., Cheng, T., and Li, X.: Seasonal contributions to size-resolved n-alkanes (C_8–C_{40}) in the Shanghai atmosphere from regional anthropogenic activities and terrestrial plant waxes, Sci. Total Environ., 579, 1918-1928, https://doi.org/10.1016/j.scitotenv.2016.11.201, 2017.

Madhu, A. and Jang, M.: Modeling the influence of carbon branching structure on SOA formation via multiphase reactions of alkanes, Zenodo [data set], https://zenodo.org/records/10667797, 2024.

Madhu, A., Jang, M., and Kim, G.: UF-atmospheric-chemistry-lab/UNIPAR_V5: UNIPAR_V5 (Version V5), Zenodo [code], https://doi.org/10.5281/zenodo.11151155, 2024.

Madhu, A., Jang, M., and Deacon, D.: Modeling the influence of chain length on secondary organic aerosol (SOA) formation via multiphase reactions of alkanes, Atmos. Chem. Phys., 23, 1661–1675, https://doi.org/10.5194/acp-23-1661-2023, 2023.

Manavi, S. E. I. and Pandis, S. N.: A lumped species approach for the simulation of secondary organic aerosol production from intermediate-volatility organic compounds (IVOCs): application to road transport in PMCAMx-iv (v1.0), Geosci. Model Dev., 15, 7731–7749, https://doi.org/10.5194/gmd-15-7731-2022, 2022.

Männistö, E., Ylänne, H., Losoi, M., Keinänen, M., Yli-Pirilä, P., Korrensalo, A., Bäck, J., Hellén, H., Virtanen, A., and Tuittila, E.-S.: Emissions of biogenic volatile organic compounds from adjacent boreal fen and bog as impacted by

vegetation composition, Sci. Total Environ., 858, 159809, https://doi.org/10.1016/j.scitotenv.2022.159809, 2023.

Massolo, L., Rehwagen, M., Porta, A., Ronco, A., Herbarth, O., and Mueller, A.: Indoor–outdoor distribution and risk assessment of volatile organic compounds in the atmosphere of industrial and urban areas, Environ. Toxicol., 25, 339-349, https://doi.org/10.1002/tox.20504, 2010.

McMurry, P. H. and Grosjean, D.: Gas and aerosol wall losses in Teflon film smog chambers, Environ. Sci. Technol., 19, 1176–1182, 1985.

Murphy, B. N., Sonntag, D., Seltzer, K. M., Pye, H. O. T., Allen, C., Murray, E., Toro, C., Gentner, D. R., Huang, C., Jathar, S., Li, L., May, A. A., and Robinson, A. L.: Reactive organic carbon air emissions from mobile sources in the United States, Atmos. Chem. Phys., 23, 13469–13483, https://doi.org/10.5194/acp-23-13469-2023, 2023.

Myrdal, P. B. and Yalkowsky, S. H.: Estimating Pure Component Vapor Pressures of Complex Organic Molecules, Ind. Eng. Chem. Res., 36, 2494–2499, https://doi.org/10.1021/ie950242l, 1997.

Nel, A.: Air Pollution-Related Illness: Effects of Particles, Science, 308, 804–806, https://doi.org/10.1126/science.1108752, 2005.

Odian, G.: Principles of polymerization, John Wiley & Sons, ISBN 9780471478751, 2004.

Pankow, J. F.: An absorption model of gas/particle partitioning of organic compounds in the atmosphere, Atmos. Environ., 28, 185–188, https://doi.org/10.1016/1352-2310(94)90093-0, 1994.

Platts, J. A., Butina, D., Abraham, M. H., and Hersey, A.: Estimation of Molecular Linear Free Energy Relation Descriptors Using a Group Contribution Approach, J. Chem. Inf. Comput. Sci., 39, 835–845, https://doi.org/10.1021/ci980339t, 1999.

Praske, E., Otkjær, R. V., Crounse, J. D., Hethcox, J. C., Stoltz, B. M., Kjaergaard, H. G., and Wennberg, P. O.: Atmospheric autoxidation is increasingly important in urban and suburban North America, P. Natl. Acad. Sci. USA, 115, 64–69, https://doi.org/10.1073/pnas.1715540115, 2018.

Press, W. H., Flannery, B. P., Teukolsky, S. A., and Vetterling, W. T.: Newton-Raphson method using derivative and Newton-Raphson method for nonlinear systems of equations, in: Numerical Recipes in FORTRAN: The Art of Scientific Computing, Cambridge University Press, ISBN 0-521-43064-X, 1992.

Puzyn, T., Leszczynski, J., and Cronin, M. T.: Recent advances in QSAR studies: methods and applications, ISBN 9781402097824, 2010.

Pye Havala, O. T., D'Ambro Emma, L., Lee Ben, H., Schobesberger, S., Takeuchi, M., Zhao, Y., Lopez-Hilfiker, F., Liu, J., Shilling John, E., Xing, J., Mathur, R., Middlebrook Ann, M., Liao, J., Welti, A., Graus, M., Warneke, C., de Gouw Joost, A., Holloway John, S., Ryerson Thomas, B., Pollack Ilana, B., and Thornton Joel, A.: Anthropogenic enhancements to production of highly oxygenated molecules from autoxidation, P. Natl. Acad. Sci. USA, 116, 6641–6646, https://doi.org/10.1073/pnas.1810774116, 2019.

Reid, J. P., Bertram, A. K., Topping, D. O., Laskin, A., Martin, S. T., Petters, M. D., Pope, F. D., and Rovelli, G.: The viscosity of atmospherically relevant organic particles, Nat. Commun., 9, 956, https://doi.org/10.1038/s41467-018-03027-z, 2018.

Roldin, P., Ehn, M., Kurtén, T., Olenius, T., Rissanen, M. P., Sarnela, N., Elm, J., Rantala, P., Hao, L., Hyttinen, N., Heikkinen, L., Worsnop, D. R., Pichelstorfer, L., Xavier, C., Clusius, P., Öström, E., Petäjä, T., Kulmala, M., Vehkamäki, H., Virtanen, A., Riipinen, I., and Boy, M.: The role of highly oxygenated organic molecules in the Boreal aerosol-cloud-climate system, Nat. Commun., 10, 4370, https://doi.org/10.1038/s41467-019-12338-8, 2019.

Sazhin, S. S., Al Qubeissi, M., Nasiri, R., Gun'ko, V. M., Elwardany, A. E., Lemoine, F., Grisch, F., and Heikal, M. R.: A multi-dimensional quasi-discrete model for the analysis of Diesel fuel droplet heating and evaporation, Fuel, 129, 238–266, https://doi.org/10.1016/j.fuel.2014.03.028, 2014.

Schell, B., Ackermann, I. J., Hass, H., Binkowski, F. S., and Ebel, A.: Modeling the formation of secondary organic aerosol within a comprehensive air quality model system, J. Geophys. Res.-Atmos., 106, 28275–28293, https://doi.org/10.1029/2001JD000384, 2001.

Shrivastava, M., Cappa, C. D., Fan, J., Goldstein, A. H., Guenther, A. B., Jimenez, J. L., Kuang, C., Laskin, A., Martin, S. T., Ng, N. L., Petaja, T., Pierce, J. R., Rasch, P. J., Roldin, P., Seinfeld, J. H., Shilling, J., Smith, J. N., Thornton, J. A., Volkamer, R., Wang, J., Worsnop, D. R., Zaveri, R. A., Zelenyuk, A., and Zhang, Q.: Recent advances in understanding secondary organic aerosol: Implications for global climate forcing, Rev. Geophys., 55, 509–559, https://doi.org/10.1002/2016RG000540, 2017.

Song, C., Liu, B., Dai, Q., Li, H., and Mao, H.: Temperature dependence and source apportionment of volatile organic compounds (VOCs) at an urban site on the north China plain, Atmos. Environ., 207, 167–181, https://doi.org/10.1016/j.atmosenv.2019.03.030, 2019.

Stein, S. E. and Brown, R. L.: Estimation of normal boiling points from group contributions, J. Chem. Inf. Comp. Sci., 34, 581–587, 1994.

Tkacik, D. S., Presto, A. A., Donahue, N. M., and Robinson, A. L.: Secondary Organic Aerosol Formation from Intermediate-Volatility Organic Compounds: Cyclic, Linear, and Branched Alkanes, Environ. Sci. Technol., 46, 8773–8781, https://doi.org/10.1021/es301112c, 2012.

Tkacik, D. S., Lambe, A. T., Jathar, S., Li, X., Presto, A. A., Zhao, Y., Blake, D., Meinardi, S., Jayne, J. T., Croteau, P. L., and Robinson, A. L.: Secondary Organic Aerosol Formation from in-Use Motor Vehicle Emissions Using a Potential Aerosol Mass Reactor, Environ. Sci. Technol., 48, 11235–11242, https://doi.org/10.1021/es502239v, 2014.

U.S. EPA: Integrated Science Assessment (ISA) for Particulate Matter (Final Report, Dec 2019), https://assessments.epa.gov/isa/document/&deid=347534 (last access: 10 December 2023), 2019.

World Health Organization (WHO): Ambient air pollution: a global assessment of exposure and burden of disease, World Health Organization, Geneva, ISBN 9789241511353, 2016.

Wu, L., Wang, X., Lu, S., Shao, M., and Ling, Z.: Emission inventory of semi-volatile and intermediate-volatility organic compounds and their effects on secondary organic aerosol over the Pearl River Delta region, Atmos. Chem. Phys., 19, 8141–8161, https://doi.org/10.5194/acp-19-8141-2019, 2019.

Xavier, C., Rusanen, A., Zhou, P., Dean, C., Pichelstorfer, L., Roldin, P., and Boy, M.: Aerosol mass yields of selected biogenic volatile organic compounds – a theoretical study with nearly

explicit gas-phase chemistry, Atmos. Chem. Phys., 19, 13741–13758, https://doi.org/10.5194/acp-19-13741-2019, 2019.

Xuan, L., Ma, Y., Xing, Y., Meng, Q., Song, J., Chen, T., Wang, H., Wang, P., Zhang, Y., and Gao, P.: Source, temporal variation and health risk of volatile organic compounds (VOCs) from urban traffic in harbin, China, Environ. Pollut., 270, 116074, https://doi.org/10.1016/j.envpol.2020.116074, 2021.

Yang, W., Li, J., Wang, W., Li, J., Ge, M., Sun, Y., Chen, X., Ge, B., Tong, S., Wang, Q., and Wang, Z.: Investigating secondary organic aerosol formation pathways in China during 2014, Atmos. Environ., 213, 133–147, https://doi.org/10.1016/j.atmosenv.2019.05.057, 2019.

Yap, C. W.: PaDEL-descriptor: An open source software to calculate molecular descriptors and fingerprints, J. Comput. Chem., 32, 1466–1474, https://doi.org/10.1002/jcc.21707, 2011.

Yu, Z., Jang, M., and Madhu, A.: Prediction of Phase State of Secondary Organic Aerosol Internally Mixed with Aqueous Inorganic Salts, J. Phys. Chem. A, 125, 10198–10206, https://doi.org/10.1021/acs.jpca.1c06773, 2021a.

Yu, Z., Jang, M., Zhang, T., Madhu, A., and Han, S.: Simulation of Monoterpene SOA Formation by Multiphase Reactions Using Explicit Mechanisms, ACS Earth and Space Chemistry, 5, 1455–1467, https://doi.org/10.1021/acsearthspacechem.1c00056, 2021b.

Yu, Z., Jang, M., Kim, S., Son, K., Han, S., Madhu, A., and Park, J.: Secondary organic aerosol formation via multiphase reaction of hydrocarbons in urban atmospheres using CAMx integrated with the UNIPAR model, Atmos. Chem. Phys., 22, 9083–9098, https://doi.org/10.5194/acp-22-9083-2022, 2022.

Zhao, L., Li, P., and Yalkowsky, S. H.: Predicting the Entropy of Boiling for Organic Compounds, J. Chem. Inf. Comp. Sci., 39, 1112–1116, https://doi.org/10.1021/ci990054w, 1999.

Zhao, Q., Bi, J., Liu, Q., Ling, Z., Shen, G., Chen, F., Qiao, Y., Li, C., and Ma, Z.: Sources of volatile organic compounds and policy implications for regional ozone pollution control in an urban location of Nanjing, East China, Atmos. Chem. Phys., 20, 3905–3919, https://doi.org/10.5194/acp-20-3905-2020, 2020.

Zhou, C., Jang, M., and Yu, Z.: Simulation of SOA formation from the photooxidation of monoalkylbenzenes in the presence of aqueous aerosols containing electrolytes under various NO_x levels, Atmos. Chem. Phys., 19, 5719–5735, https://doi.org/10.5194/acp-19-5719-2019, 2019.

Zuend, A., Marcolli, C., Booth, A. M., Lienhard, D. M., Soonsin, V., Krieger, U. K., Topping, D. O., McFiggans, G., Peter, T., and Seinfeld, J. H.: New and extended parameterization of the thermodynamic model AIOMFAC: calculation of activity coefficients for organic-inorganic mixtures containing carboxyl, hydroxyl, carbonyl, ether, ester, alkenyl, alkyl, and aromatic functional groups, Atmos. Chem. Phys., 11, 9155–9206, https://doi.org/10.5194/acp-11-9155-2011, 2011.